INORGANIC CHEMISTRY FRONTIERS

RESEARCH ARTICLE

View Article Online
View Journal | View Issue



Cite this: *Inorg. Chem. Front.*, 2024, **11**, 882

# Manipulating the crystallization and interfacial charge behavior with a jellyfish-like molecular template for efficient perovskite solar cells†

Haoyan Wang,[a] Chenyu Zhao,[a] Lin Fan,[a,b] Maobin Wei,[a,b] Huilian Liu,[a,b] Xiaoyan Liu,[a,b] Jinghai Yang,*[a,b] Fengyou Wang*[a,b] and Lili Yang*[a,b]

The buried electron-transport layer (ETL)/perovskite interface is crucial for the performance of n-i-p-type perovskite solar cells. However, the presence of nonuniform distributed dangling bonds on the mainstream metal oxide ETL surface leads to nonradiative recombination and affects the homogenization of the perovskite film by triggering disordered nucleation. To address these challenges, we modulated the ETL/perovskite interface by introducing a jellyfish-like molecular template (JLMT), where the jellyfish foot was glycine and the jellyfish head was $MoS_2$, to simultaneously achieve highly oriented perovskite films and efficient interfacial charge transfer. Glycine was first anchored on the ETL through esterification. Then, sequentially layered $MoS_2$ was deposited on the surface. The lower reduction potential of glycine with respect to that of $MoS_2$ drives electron transfer from glycine to $MoS_2$, leading to surface charge doping and building a favorable bandgap alignment at the ETL/perovskite interface. In addition, the top surface of $MoS_2$, which is free from dangling bonds, could guide the orientational growth of the perovskite because of its lattice structural compatibility. An as-fabricated JLMT device achieved a champion power conversion efficiency (PCE) of 21.76% and an open-circuit voltage ($V_{oc}$) of 1.20 V. Furthermore, under room temperature conditions with a relative humidity of ~30%, the PCE of the JLMT device retained 93% of its initial value after 30 days, whereas the control device only retained around 61% of its initial PCE.

Received 3rd October 2023,
Accepted 9th December 2023

DOI: 10.1039/d3qi02016a

rsc.li/frontiers-inorganic



## 1. Introduction

In just a dozen years, the power conversion efficiency (PCE) of perovskite solar cells (PSCs) has skyrocketed rapidly from 3.8% to 26.1% (certified in 2023) owing to their high optical absorption coefficient and long carrier diffusion length (>1 μm).[1,2] In regular-structure (n-i-p) planar perovskite solar cells (PSCs), the perovskite absorption layer, primarily prepared through a solution process, is sandwiched between the electron-transport layer (ETL) and the hole-transport layer (HTL). The ETL/perovskite interface is crucial because it not only affects the nucleation and growth process of the perovskite but also dominates photogenerated electron extraction and transfer.[3] Various metal oxides ($TiO_2$, $SnO_2$, ZnO, *etc.*) are selected as ETLs due to their excellent electron mobility, high light transmittance, and good band alignment with perovskite.[4] However, during the preparation process, the formation of metal oxide ETLs leads to inevitable valence bond breaking (specifically, metal–oxygen bonds), resulting in a nonuniform distribution of dangling bonds on the surface. These dangling bonds can adversely affect the homogenization of the perovskite film by inducing disordered nucleation.[5] In addition, recent studies have found that dangling bonds existing on the surfaces of metal oxides can interact with moisture to form hydroxyl (–OH) groups, which act as Brønsted bases and undergo a deprotonation reaction with the perovskite, leading to a deterioration in its framework and stability.[6] Meanwhile, dangling bond defects can also induce interfacial carrier nonradiative recombination, hindering further enhancement of the PCE and stability of PSCs.[7] Therefore, terminating dangling bonds on the surface of metal oxides is a key factor in improving perovskite crystallization and stability and accelerating carrier transport to achieve high-performance PSCs.

Several carboxyl-containing molecules, such as amino acids, carboxylic acids, and diethanolamine, have been self-assembled on ETLs (metal oxides) by esterification to mini-

[a]*Key Laboratory of Functional Materials Physics and Chemistry of the Ministry of Education, Jilin Normal University, Changchun 130103, China. E-mail: jhyang1@jlnu.edu.cn, wfy@jlnu.edu.cn, llyang1980@163.com*
[b]*National Demonstration Center for Experimental Physics Education, Jilin Normal University, Siping 136000, China*

†Electronic supplementary information (ESI) available. See DOI: https://doi.org/10.1039/d3qi02016a

mize interfacial dangling bonds.[8–10] However, the film homogeneity can be influenced by the nonuniform distribution of extra groups or chemical bonds in the modifiers. In addition to organic groups, many inorganic materials such as carbon-based materials[11–15] and metallic compounds are employed to modify the perovskite interface. In an earlier study, we introduced an inorganic amorphous metal nitride (a-$TiN_x$) layer at the ETL/perovskite interface to eliminate the dangling bonds through coordination interactions with nitride atoms.[16] However, due to the uncertain valence states of the metal ions in the amorphous state, uncoordinated metal ions still exist on the surface of the a-$TiN_x$ interlayer, resulting in the formation of dangling bonds.

In addition to the aforementioned approaches, van der Waals (vdW) epitaxy is also a common technique for preparing high-quality semiconductor films with preferential orientations on smooth and dangling-bond-free surfaces.[17–20] Inspired by these intriguing effects, 2D materials with proper lattice parameters have been utilized as growth templates for preparing high-quality perovskite films with a controllable orientation and less defect interface, thereby improving photovoltaic performance and stability. As a typical representative, molybdenum disulfide ($MoS_2$) is a promising 2D transition metal dichalcogenide (TMD) with a dangling-bond-free surface and a matched lattice with perovskite. The interplane distances of $MAPbI_3$ (008) and $MoS_2$ (110) planes have an identical value of 1.58 Å, which lays a foundation for perovskite epitaxy growth.[21,25]

However, it is worth noting that the energy level of $MoS_2$ (~3.4–5.2 eV) is mismatched with the perovskite in n-i-p PCSs, and an unfavorable bandgap offset will thus be established at the $MoS_2$/perovskite interface, hindering the interfacial carrier transfer.[23] Fortunately, previous studies have demonstrated that surface charge doping by strong electron-donating groups can alter the Fermi level and subsequently adjust the energy level structure of $MoS_2$, which is promising for achieving energy level alignment between $MoS_2$ and perovskite.[24–27]

Accordingly, in this work, a jellyfish-like molecular template (JLMT), where the jellyfish foot was glycine and the jellyfish head was $MoS_2$, was developed to modulate the ETL/perovskite interface for simultaneously achieving highly oriented perovskite films and boosting the interfacial charge transfer. Glycine was first anchored on the $SnO_2$ ETL through esterification; then, $MoS_2$ was absorbed on the glycine by solution spin coating. The lower reduction potential of glycine with respect to that of $MoS_2$ drives electron transfer from glycine to $MoS_2$, forming surface charge doping and building a favorable bandgap alignment at the ETL/perovskite interface. Notably, the surface charge doping did not induce any dangling bonds in $MoS_2$ lattice, which maintained the oriented epitaxial growth of perovskite on the $MoS_2$ surface. An as-fabricated JLMT PSC exhibited a significantly improved photovoltaic performance and reduced hysteresis behavior, yielding a champion PCE of 21.76% accompanied by an open-circuit voltage ($V_{oc}$) of 1.20 V, which is one of the highest PCEs for $MAPbI_3$ solar cells. Meanwhile, the PCE retained 93% of its value under room temperature conditions with a relative humidity (RH) of 30% compared with the control devices after 30 days.

## 2. Results and discussion

To confirm the phase of the $MoS_2$ nanosheet, we conducted X-ray diffraction (XRD) and Raman spectroscopy analyses of the samples. The XRD pattern of the target $MoS_2$ nanosheet was matched with the standard diffraction pattern of the 2H-phase layered $MoS_2$ file (JCPDS#37-1492). Three diffraction peaks centered at 14.5°, 32.9°, and 58.5° could be observed, corresponding to the (002), (100), and (110) planes of $MoS_2$ nanosheet.[28] The Raman spectrum showed the presence of two peaks at ~378 $cm^{-1}$ and ~402 $cm^{-1}$, which corresponded to the in-plane $E_{2g}$ and out-of-plane $A_{1g}$ vibration modes of the 2H-phase $MoS_2$.[22,29] Subsequently, we explored the structure information using transmission electron microscopy (TEM) and high-resolution transmission electron microscopy (HRTEM). As shown in Fig. 1c, the TEM image revealed the layered structure of $MoS_2$. Energy-dispersive X-ray spectroscopy (EDS) analysis confirmed the uniform distribution of both Mo and S elements within the layered $MoS_2$ structure (Fig. S1†). Further analysis using HRTEM allowed the clear identification of lattice fringes with a spacing of 0.316 nm, corresponding to the (004) plane of 2H $MoS_2$ (inset in Fig. 1c).[29,30] To determine the thickness of the $MoS_2$ nanosheet, atomic force microscopy (AFM) was employed. The AFM image, as shown in Fig. S2,† indicated an average thickness of ~1.5 nm.

The growth of $MAPbI_3$ on $MoS_2$ surface was further monitored. $MoS_2$ nanosheets were drop-coated on a carbon-coated copper grid; then a precursor solution of $MAPbI_3$ was spin-coated on the sample surfaces and solidified by an anti-solvent method, followed by thermal annealing at 100 °C for 10 min, which was similar to the perovskite film preparation procedure in PSCs. Next, the samples were characterized using HRTEM. Fig. 2a shows the typical TEM image of the as-synthesized heterostructure in which the $MAPbI_3$ film can be seen to be partially covering the surface of a $MoS_2$ nanosheet. Fig. 2b and c show the HRTEM images of the $MoS_2$ and $MAPbI_3$ regions, respectively. The presence of clear lattice fringes indicated the high quality of both the $MoS_2$ nanosheet and the $MAPbI_3$ grain. The lattice fringe with a distance of 1.58 Å corresponded to the (110) plane of $MoS_2$, while the lattice fringe with a distance of 3.16 Å corresponded to the (004) plane of the $MAPbI_3$ grain. Fig. 2d and e display the selected area electron diffraction (SAED) patterns of pure $MoS_2$ and $MAPbI_3$, respectively, which serve as reference patterns. The SAED pattern of the overlapping area between $MAPbI_3$ and $MoS_2$ revealed the relative crystallographic orientation of the $MAPbI_3$ layer and $MoS_2$ crystal in the heterostructure (Fig. 2f). The SAED pattern exhibited two sets of diffraction spots with square (red) and hexagonal (yellow) symmetries. Each diffraction spot in the smaller and larger hexagonal patterns corresponded to the (100) and (110) family planes of the $MoS_2$ crystal, respectively. Each diffraction spot in the square pattern could be indexed to

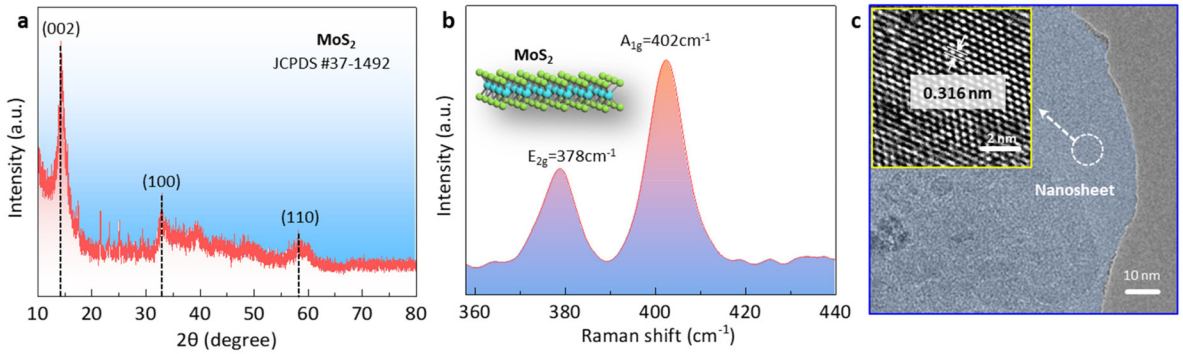


**Fig. 1** Properties of the $MoS_2$ nanosheets. (a) XRD pattern, (b) Raman spectra, and (c) TEM and HRTEM images.



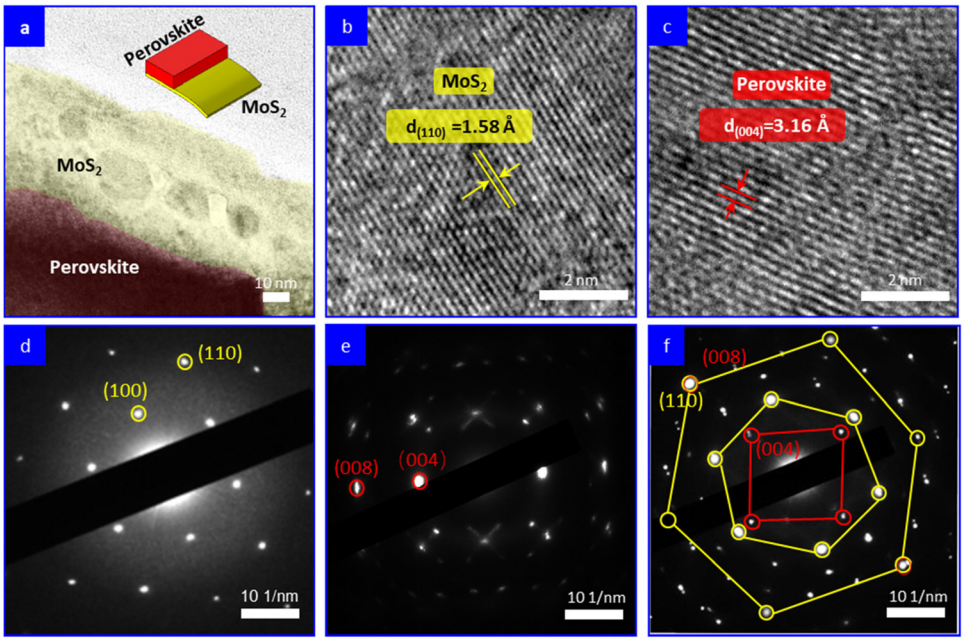


**Fig. 2** $MAPbI_3$ epitaxially grown on $MoS_2$. (a) Top-view TEM image of $MoS_2$ with a $MAPbI_3$ layer grown on its surface. (b and c) HRTEM images of $MoS_2$ and $MAPbI_3$, respectively. (d and e) SAED patterns of $MoS_2$ and $MAPbI_3$ as reference patterns, respectively. (f) SAED pattern of $MAPbI_3/MoS_2$ region, where two distinct diffraction spots can be observed, with the yellow spots representing $MoS_2$ and the red spots representing $MAPbI_3$.

the (004) family plane of the $MAPbI_3$ layer. Intriguingly, based on the literature,[19,21] it is worth noting that the interplane distances of the (008) plane of $MAPbI_3$ and the (110) plane of $MoS_2$ are identical, measuring 1.58 Å. Consequently, this suggests that the in-plane coupling between $MoS_2$ and $MAPbI_3$ may facilitate the preferential growth of $MAPbI_3$ grains along the (110) plane on the surface of the $MoS_2$ templates. This concept is schematically illustrated in Fig. S3.† In Fig. 2f, it can be observed that the (008) plane of $MAPbI_3$ perfectly overlapped with the (110) plane of $MoS_2$, providing evidence for the impeccable lattice match between these two planes. Thus, it confirms that the $MAPbI_3$ layer exhibited epitaxial growth on the $MoS_2$ nanosheet.

Scanning electron microscopy (SEM) and X-ray diffraction (XRD) were used to investigate the crystallization of $MAPbI_3$ grown on $MoS_2$. The SEM analysis revealed that the $MAPbI_3$ film grown on the $MoS_2$ substrate ($MoS_2$-$MAPbI_3$) exhibited larger grains and fewer boundaries compared with the control film grown on the $SnO_2$ substrate. The grain size of $MAPbI_3$ increased by ~300 nm when grown on $MoS_2$, indicating the improved crystallization (Fig. 3a and Fig. S4†). Next, X-ray diffraction (XRD) measurements were performed to study the crystal orientation of $MAPbI_3$. The (110) peak intensity of the $MoS_2$-$MAPbI_3$ film was markedly stronger than that of the control film (7085.53 a.u. *versus* 5176.65 a.u.). The increased relative intensity of (110)/(310) (from 5.42 to 6.93 a.u.) suggested the preferential orientation along the (110) direction[21,30] (Fig. 3b). Further analysis was conducted using grazing incidence wide-angle X-ray scattering (GIWAXS) on the corresponding films to examine the effect of $MoS_2$ on the

 

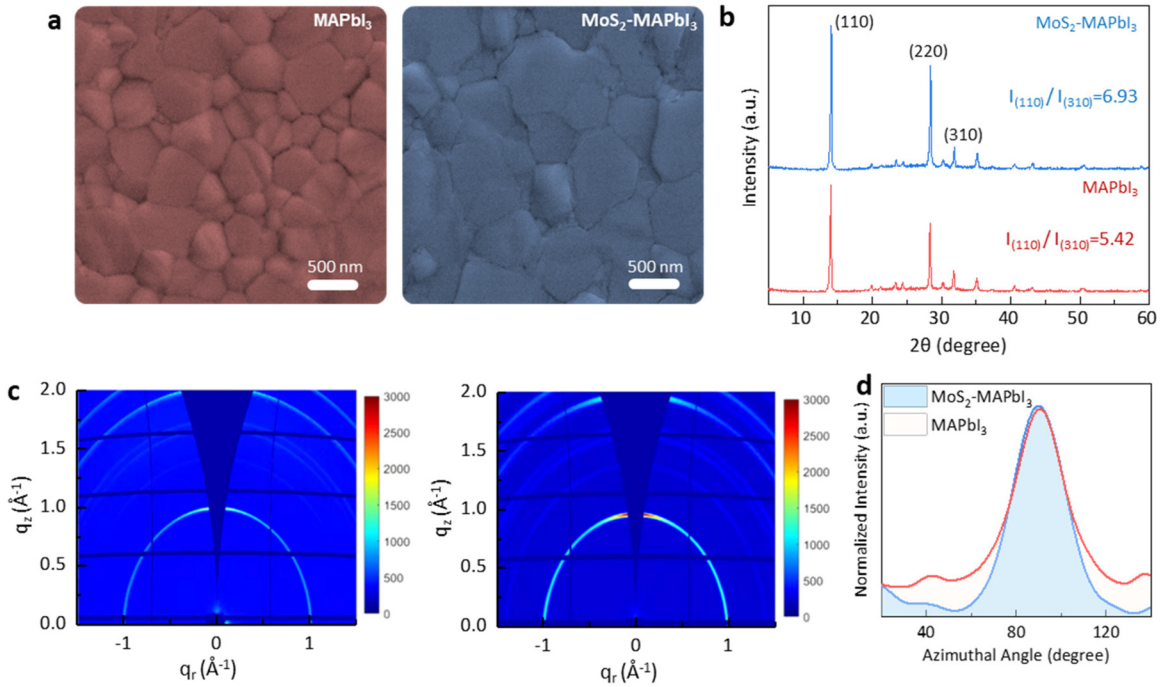


**Fig. 3** Crystallization of $MoS_2$-$MAPbI_3$. (a) SEM images of the $MAPbI_3$ and $MoS_2$-$MAPbI_3$ films. (b) XRD patterns of the $MAPbI_3$ film and $MoS_2$-$MAPbI_3$ film. (c) 2D GIWAXS patterns for the $MAPbI_3$ and $MoS_2$-$MAPbI_3$ films. (d) Azimuthal pole plot of (110) diffraction for the $MoS_2$-$MAPbI_3$ and $MAPbI_3$ films prepared under the same conditions.

crystal orientation of $MAPbI_3$. Fig. 3c shows the 2D GIWAXS patterns of the $MAPbI_3$ and $MoS_2$-$MAPbI_3$ films. Compared to the $MAPbI_3$ film, the $MoS_2$-$MAPbI_3$ film exhibited a more distinct diffraction ring at $q$ = 1 $Å^{-1}$, which corresponded to the (110) plane. The intensity distribution range around the azimuthal angle of 90° was narrower for the $MoS_2$-$MAPbI_3$ films, indicating an improved orientation of the $MoS_2$-$MAPbI_3$ films (Fig. 3d).[21] These observed phenomena could be attributed to two factors: (1) the matching lattice structure between the (008) plane of $MAPbI_3$ and the (110) plane of $MoS_2$, which promoted the growth of $MAPbI_3$ along the (110) plane; and (2) the dangling-bond-free surface of $MoS_2$, which facilitated the migration of radicals and increased the grain boundary mobility. This accelerated the lateral growth of perovskite grains and led to an enlargement of the perovskite grain size.[20,30]

Furthermore, planar perovskite solar cells with an architecture of Glass/ITO/$SnO_2$/with- and without $MoS_2$/$MAPbI_3$/Spiro-OMeTAD/Ag were fabricated (Fig. 4a). Typically, an improved perovskite crystallinity leads to increased device efficiency due to the presence of fewer defects and reduced nonradiative recombination. However, the statistical analysis of 20 devices (10 $MAPbI_3$-devices and 10 $MoS_2$-$MAPbI_3$-devices) showed that the PCE, as well as the other key parameters of the devices (*i.e.*, $V_{oc}$, $J_{sc}$, FF), decreased from 18.59 ± 0.3% to 17.24 ± 0.4% following $MoS_2$ application (Fig. 4b–e). Since the preparation process of the devices with and without $MoS_2$ was the same, we suspected that the decreased PCE may be related to the interface properties. Previous work has shown that the energy level of $MoS_2$ (~3.4–5.2 eV) is mismatched with that of $MAPbI_3$ (~3.9–5.4 eV),[31,32] resulting in an interfacial energy barrier that blocks charge transport and further reduces device efficiency. To validate this assumption, we measured the ultraviolet photoelectron spectra (UPS) and UV-vis absorption spectra of $MoS_2$ and $MAPbI_3$, respectively. The conduction band ($E_C$), Fermi energy ($E_F$), and valence band ($E_V$) of $MoS_2$ were −3.46, −4.58, and −5.20 eV, while those of $MAPbI_3$ were −3.93, −4.50, and −5.43 eV, respectively (Fig. S5 and S6†). Therefore, the energy level structure between $MoS_2$ and $MAPbI_3$ can be depicted as shown in Fig. 4f. Under thermal equilibrium, a band offset is formed, which hinders electron extraction and decreases the device PCE.

Accordingly, it is crucial to realign the energy level structure of $MoS_2$ to enhance electron extraction at the $MoS_2$-$MAPbI_3$ interface and further improve device performance. Chemical doping is a common approach for regulating the energy levels and electronic properties of different types of transition metal dichalcogenides (TMDCs), including $MoS_2$ and $WSe_2$. In particular, surface-charge-transfer doping, achieved by adsorbing specific electron-donating or electron-withdrawing groups on the surfaces of TMDCs, has been demonstrated as an effective method in previous studies. For instance, Javey *et al.*[25] utilized benzyl viologen (BV) as a surface-charge-transfer donor for $MoS_2$ flakes to regulate their energy levels. The high reduction potentials of BV promoted electron transfer from BV molecules to $MoS_2$ flakes, resulting in n-type doping and an elevation of the Fermi level in the $MoS_2$ flakes. Similarly, Du *et al.* achieved

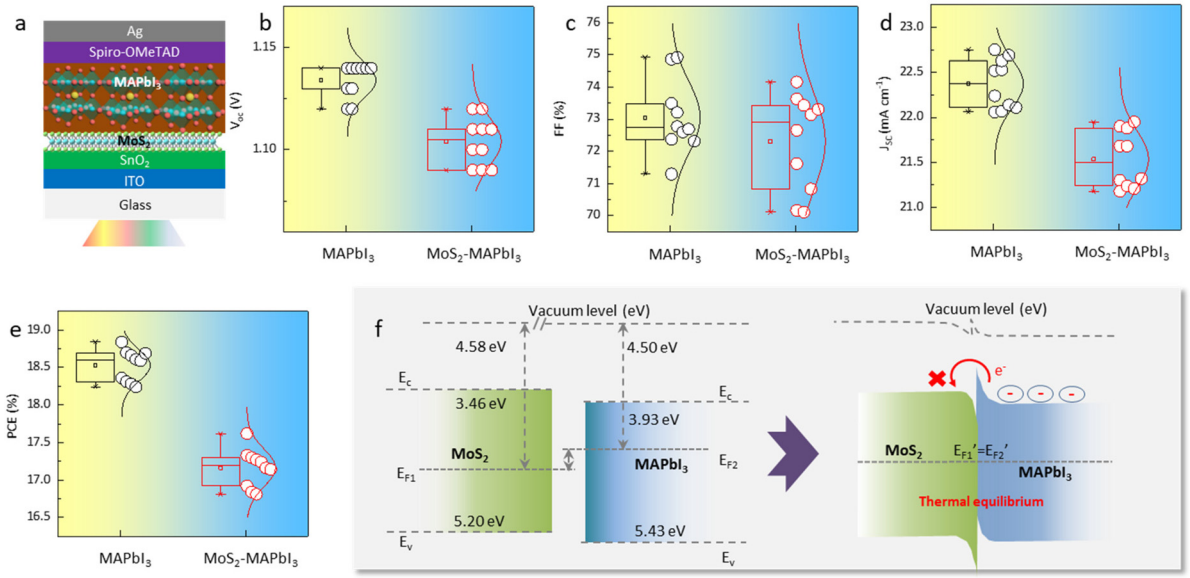


**Fig. 4** Bandgap alignment between $MoS_2$ and $MAPbI_3$. (a) Schematic structure of the $MoS_2$-$MAPbI_3$ device. (b–e) Distribution of $V_{OC}$, $J_{SC}$, FF, and PCE values collected from 10 $MAPbI_3$ and 10 $MoS_2$-$MAPbI_3$ devices. (f) Energy level change scheme of $MoS_2$ and $MAPbI_3$.

n-type doping in $MoS_2$ by immersing it in an amine-rich aliphatic polymer (PEI) solution.[33] This realignment of energy levels led to reduced sheet resistance and contact resistance in multilayer $MoS_2$ field-effect transistors.

In this work, it was important to note that this doping method may introduce additional functional groups on the both sides of the $MoS_2$ layer, which could disrupt the templating function of $MoS_2$ and affect the epitaxial growth of $MAPbI_3$.[25,34] To overcome this challenge, we employed glycine as the dopant and proposed a single-side bonding method to construct a jellyfish-like molecular template (JLMT), where glycine served as the jellyfish foot, and $MoS_2$ as the jellyfish head (Fig. 5a). The preparation process is illustrated in Fig. 5b. Initially, glycine was anchored on the $SnO_2$ substrate through esterification between the –COOH group of glycine and the –OH group on the $SnO_2$ surface. Subsequently, $MoS_2$ was

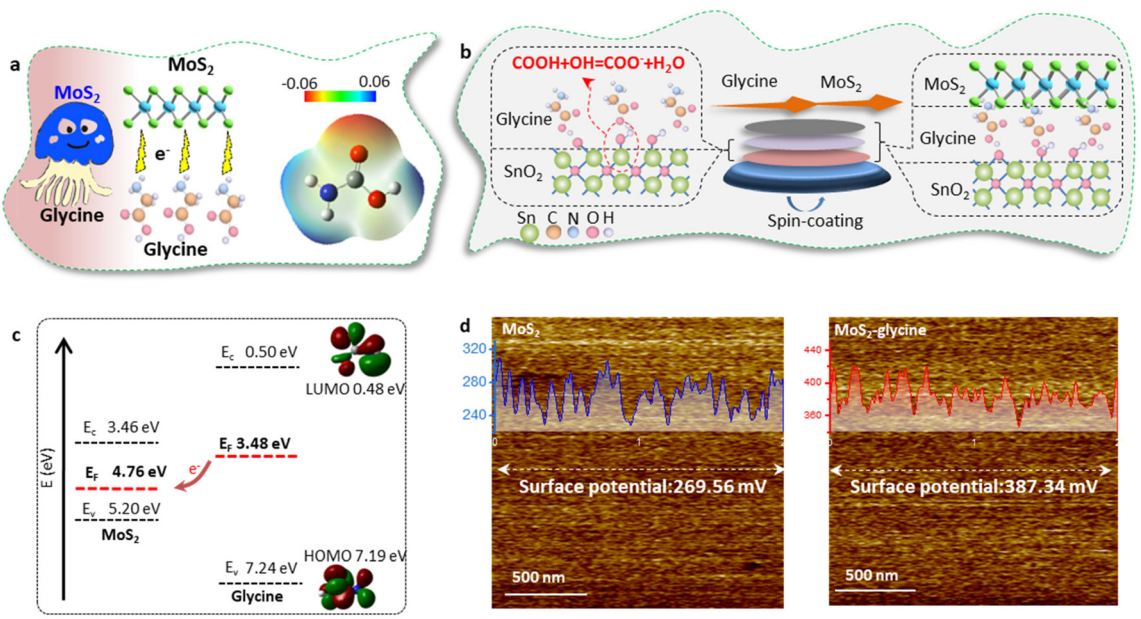


**Fig. 5** Formation mechanism of JLMT (a) Jellyfish-like structure consisting of $MoS_2$ and glycine. (b) Preparation method used to construct the JLMT (c) Electron-transfer scheme between $MoS_2$ and glycine. (d) KPFM mapping of $MoS_2$ and $MoS_2$-glycine. Inset: CPD profile along the horizontal marked lines.

 

coated on the substrate and absorbed onto the glycine surface. Fig. S7† shows the lowest occupied molecular orbital (LUMO), Fermi level ($E_F$), and the highest occupied molecular orbital (HOMO) of glycine, which were −0.50 eV, −3.48 eV, and −7.24 eV, respectively. Additionally, the HOMO and LUMO energies of glycine were determined using density functional theory calculations, as shown in Fig. 5c; these values were consistent with the measured results (HOMO: −7.19 eV and LUMO: −0.48 eV). The energy diagram illustrated in Fig. 5c displays the energy levels of both $MoS_2$ and glycine. Owing to its higher ionization potential and LUMO level, glycine acts as an electron donor to $MoS_2$, leading to alterations in its internal electron arrangement as well as changes in its energy level structure (as depicted in Fig. 5c).[35] To validate the above proposition, Kelvin probe force microscopy (KPFM) was used to characterize the surface potentials of $MoS_2$ and $MoS_2$-glycine (Fig. 5d). The contact potential difference (CPD) of $MoS_2$ was measured as 269.56 mV, whereas that of $MoS_2$-glycine increased to 387.34 mV, indicating an upward shift in the $E_F$ of $MoS_2$.[36]

Moreover, the formation mechanism of JLMT was also investigated in detail. We first used X-ray photoelectron spectroscopy (XPS) to study the esterification between $SnO_2$ and glycine. The Sn 3d XPS peaks of glycine-$SnO_2$ shifted to higher binding energies compared with the pure $SnO_2$ film (Fig. 6a). In addition, the O 1s spectrum of the pristine $SnO_2$ film plotted in Fig. 6b showed a broad asymmetric peak, which could be deconvoluted into lattice oxygen (530.34 eV) and chemisorbed oxygen atoms or hydroxyl groups (531.25 eV). The peak intensity of the lattice oxygen decreased while that of the adsorbed oxygen increased (Fig. 6c), demonstrating the change in the chemical circumstance of oxygen atoms in the lattice of $SnO_2$ surface after the treatment. These results support the view that glycine was successfully anchored on to $SnO_2$ by esterification. Fourier-transform infrared spectroscopy (FTIR) was performed and the high-resolution Mo 3d and S 2p core level XPS spectra were recorded to explore the interaction between $MoS_2$ and glycine. After depositing $MoS_2$ on glycine, the N–H vibrations of glycine were red-shifted from 1634 and 3436 $cm^{-1}$ to 1629 and 3430 $cm^{-1}$ (Fig. 6d). The XPS spectra

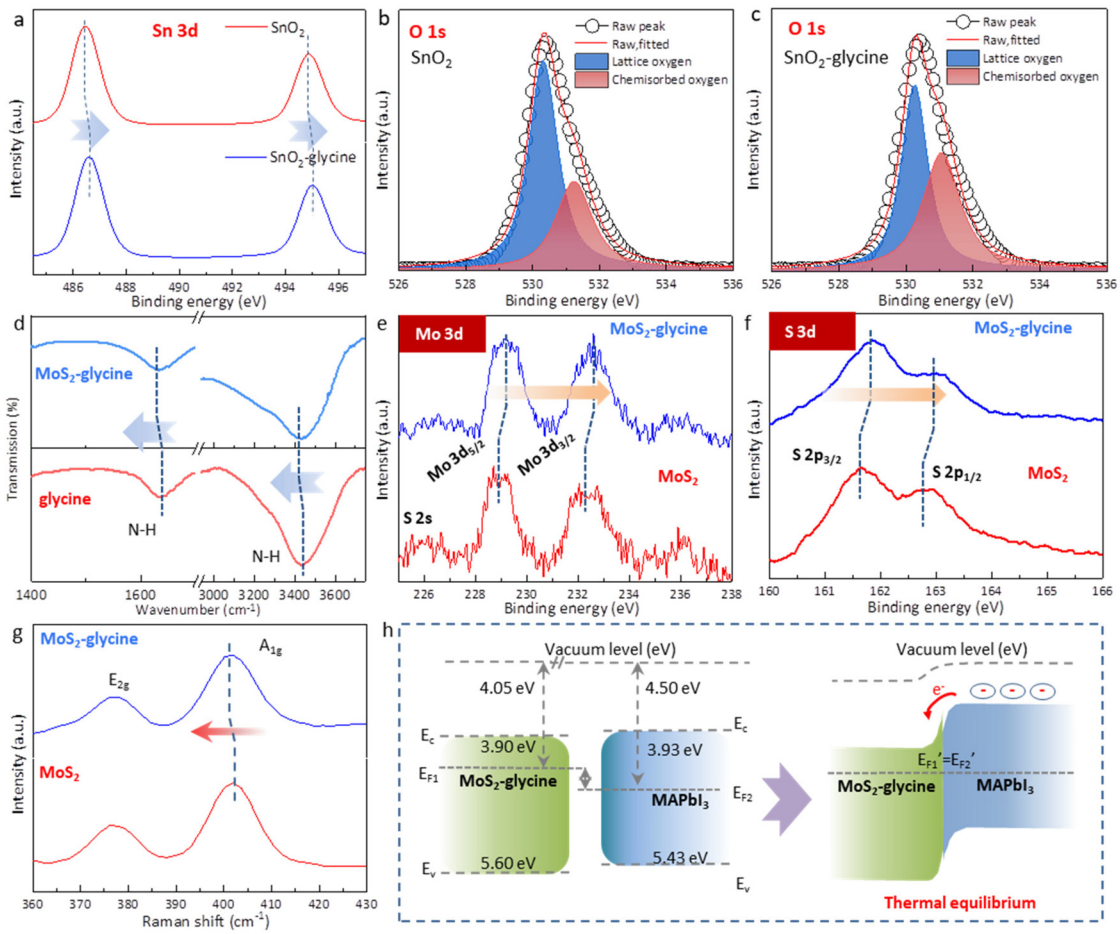


**Fig. 6** Interactions between glycine, $SnO_2$, and $MoS_2$. (a) XPS spectra of the Sn 3d signals of $SnO_2$ and $SnO_2$-glycine. (b and c) XPS spectra of the O 1s of $SnO_2$ and $SnO_2$-glycine. (d) FTIR spectra of glycine and $MoS_2$-glycine. (e and f) XPS spectra of the Mo 3d and S 3d signals for $MoS_2$ and $MoS_2$-glycine, respectively. (g) Raman shifts of $MoS_2$ and $MoS_2$-glycine. (h) Schematic diagram of the bandgap alignment at the $MoS_2$-glycine/$MAPbI_3$ interface.

showed that the characteristic peaks of the $Mo^{4+}$ $3d_{3/2}$ and $Mo^{4+}$ $3d_{5/2}$ doublets of pure $MoS_2$ located at 232.5 and 229.0 eV were shifted to a higher binding energy after depositing on glycine (Fig. 6e). Similarly, the S $2p_{3/2}$ and $2p_{1/2}$ peaks were also shifted to higher binding energies (Fig. 6f). These results imply that the $E_F$ of $MoS_2$ experienced an upward shift to the $E_C$ due to the surface-charge-transfer doping.[37,38] Raman spectroscopy was also performed to explore the electronic information of $MoS_2$ (Fig. 6g). The peak at ~378 $cm^{-1}$ corresponded to the $E_{12g}$ mode and was due to the displacement of Mo and S atoms within the basal plane, whereas the $A_{1g}$ mode at ~402 $cm^{-1}$ originated from the vibration perpendicular to the basal plane.[39] Several studies have suggested that the $E_{12g}$ mode is almost inert, but the $A_{1g}$ mode of $MoS_2$ will undergo a red-shift after n-type doping. In this case, a small red-shift of ~0.3 $cm^{-1}$ was observed for the $A_{1g}$ mode when $MoS_2$ was layered on the glycine, indicating successful n-type doping.[40] UPS was measured to further quantify the energy level of the glycine-doped $MoS_2$ (Fig. S8†). After treatment with glycine, the $E_F$ of $MoS_2$ increased from −4.58 to −4.05 eV, indicating n-type doping and supporting the aforementioned conclusion. The energy level structure diagram of $MoS_2$-glycine and $MAPbI_3$ is depicted in Fig. 6h. Under thermal equilibrium, the alignment of the energy levels between $MoS_2$-glycine and $MAPbI_3$ creates a charge-transfer channel. This interface energy level structure is more conducive to electron extraction and hole blocking, alleviating the previously mentioned problem of interface energy level mismatch and thus improving the efficiency of interface charge transfer. The PL intensity of the JLMT-$MAPbI_3$ device was weaker than that of the control device, while the TRPL lifetime with JLMT-$MAPbI_3$ was shorter. Details on the lifetime parameters are summarized in Table S1.† These findings verified that the introduction of the JLMT accelerated carrier extraction, which could be attributed to a reduction in the interfacial energy barrier at the ETL/perovskite interface.[36]

Planar PSCs were fabricated with an ITO/$SnO_2$/JLMT/$MAPbI_3$/Spiro-OMeTAD/Ag structure (Fig. 7a). The cross-sectional SEM of the JLMT device showed large grains throughout the perovskite layer compared with the control device (Fig. 7b). The control device showed a PCE of 18.48% with a hysteresis index (HI = $(PCE_{reverse} - PCE_{forward})/PCE_{reverse}$) of 7.41%. The champion PCE of the JLMT device increased to 21.76% with an HI value of 1.19% (Fig. 7c). The $V_{oc}$, $J_{sc}$, and FF values were also improved and are summarized in Table S2.† The mean and standard deviation (SD) values of the key parameters of the PSCs are shown in Table S3.† As mentioned above, the introduction of the JLMT created a more favorable bandgap alignment and minimized the energy barriers, leading to enhanced charge extraction and reduced charge recombination at the ETL/perovskite interface. These improvements significantly contributed to the enhancement of the $J_{sc}$ and FF values. Moreover, in terms of the $V_{oc}$, the use of the JLMT contributed to improved perovskite crystallization and a reduction in interface defects between the $SnO_2$ and perovskite layers. This effect minimized the charge trapping sites both in the bulk of the perovskite and at the ETL/perovskite interface. As a result, the JLMT promoted more efficient charge separation

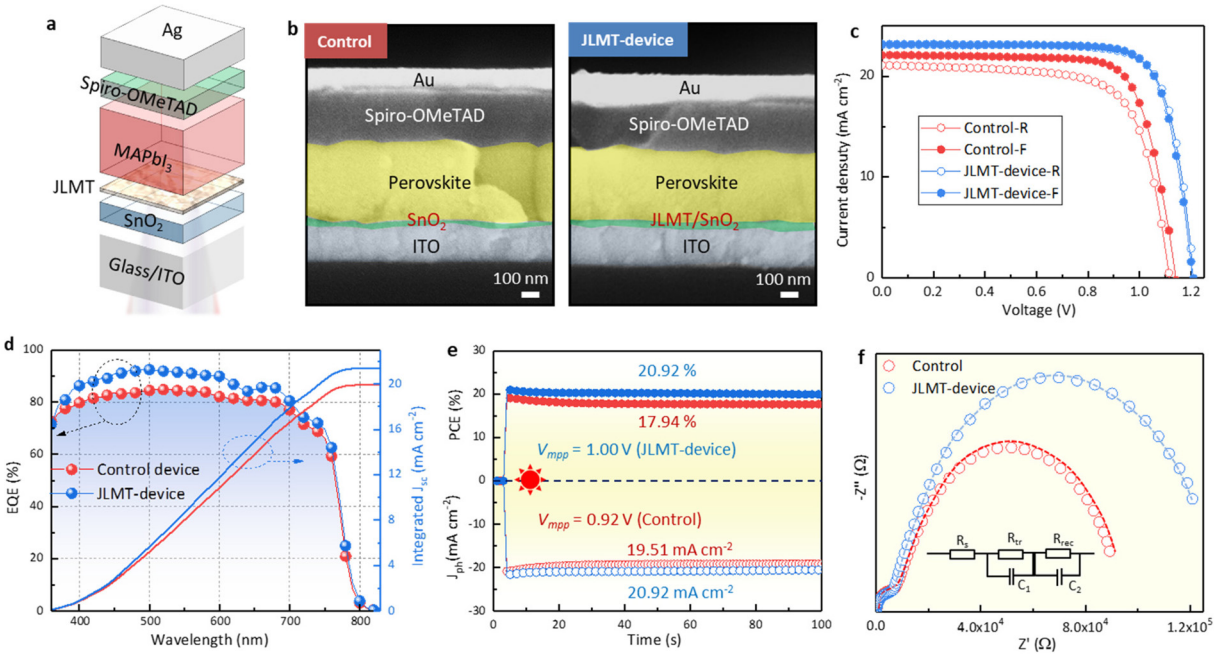


Fig. 7 Device performance (a) Whole device structure. (b) Cross-sectional SEM images of the control and JLMT devices. (c) Illuminated $J$–$V$ curves of the control and JLMT devices. (d) EQE spectra and integrated photocurrent of the control and JLMT devices. (e) PCE and output current density measured at the $V_{mpp}$ of the control and JLMT devices. (f) Nyquist plots of the control and JLMT devices. The inset shows the equivalent circuit model.

 

and reduced the nonradiative recombination, ultimately leading to an enhanced $V_{oc}$. The integrated $J_{sc}$ values obtained from the external quantum efficiency (EQE) spectra (Fig. 7d) were 19.94 and 21.41 mA $cm^{-2}$ for the control and JLMT devices, respectively, which were consistent with the tendency of the *J–V* results. The operational stabilities of the control and JLMT devices were examined under the maximum power point voltage ($V_{mpp}$), respectively. The stabilized PCE of the champion JLMT device reached 20.92% at a $V_{mpp}$ of 1.00 V, along with a photocurrent density ($J_{ph}$) of 20.92 mA $cm^{-2}$, whereas that of the control device was 17.94% at a maximum power point voltage of 0.92 V, along with a $J_{ph}$ of 19.51 mA $cm^{-2}$ (Fig. 7e).

The main reason for the improved photovoltaic performance of the device was the improvement of the crystal quality of the perovskite by the JLMT, which reduced the recombination losses within the device. Simultaneously, the cascaded energy level structure between the JLMT and perovskite also facilitated the efficient extraction of photogenerated charges, thereby reducing the charge-transfer resistance. To verify this statement, electrochemical impedance spectroscopy (EIS) was performed to explore the influence of the JLMT on the carrier-transfer behavior (Fig. 7f). The two semicircles in the inset of Fig. 7f correspond to the high-frequency transfer resistance ($R_{tr}$) and low-frequency recombination resistance ($R_{rec}$), respectively. Compared with the control device, the JLMT device showed a lower $R_{tr}$ and a higher $R_{rec}$, corresponding to faster carrier transfer and reduced recombination.[42] The fitting parameters are summarized in Table S4.†

In addition to evaluating the photovoltaic performance of the device, it is crucial to consider the long-term stability of perovskite solar cells during their development. To assess film stability, we conducted a series of tests. The XRD patterns of the control and JLMT-$MAPbI_3$ films were measured after exposure to ~40% relative humidity and a temperature of ~25 °C for 30 days (Fig. S10†). The $MAPbI_3$ film showed a $PbI_2$ peak at around 12.5°, while the JLMT-$MAPbI_3$ film showed a much lower $PbI_2$ peak, indicating the improved stability of the JLMT-$MAPbI_3$ film. Under similar environmental conditions, the UV-vis absorption spectrum revealed that the JLMT-$MAPbI_3$ film experienced a lower intensity reduction compared to the $MAPbI_3$ film (Fig. S11†). To further evaluate device stability, we monitored the unencapsulated JLMT devices at room temperature (RH ~30%) by assessing their PCE (Fig. S12†). The control device retained only 61% of its initial PCE, whereas the JLMT device exhibited superior stability, retaining ~93% of its initial PCE after 30 days. We identified three main factors contributing to the decomposition of perovskite solar cells:[41,42] ion migration induced by intrinsic defects, deprotonation reactions between the ETL surface hydroxyl groups and the perovskite layer, and moisture infiltration. In this study, the incorporation of the JLMT proved to be highly effective in suppressing deprotonation reaction-induced perovskite decomposition. This was achieved by eliminating the hydroxyl groups on the surface of $SnO_2$ and creating a clear isolation between the $SnO_2$ and perovskite layers. Moreover, by enhancing the crystallization quality of the perovskite, we were able to significantly decrease defect formation and reduce the density of grain boundaries. Consequently, this approach successfully minimized ion migration and hindered moisture infiltration, ultimately leading to a remarkable improvement in the stability of the device.

## 3. Conclusions

In summary, we used glycine and $MoS_2$ to construct a JLMT to achieve highly crystallized perovskite films and efficient interfacial charge transfer. The successful templating effect was achieved due to several factors. First, the interplane distances of the (008) plane of $MAPbI_3$ perovskite and the (110) plane of $MoS_2$ were found to be identical at 1.58 Å. Additionally, the top surface of $MoS_2$ had no dangling bonds at the $MoS_2$/perovskite interface, further facilitating the orientational growth of the perovskite due to its matched lattice structure. Moreover, glycine played a crucial role in the system. As an electron donor to $MoS_2$, the addition of glycine led to alterations in its internal electron arrangement and changes in its energy level structure. This established a favorable bandgap alignment with the perovskite, enhancing the photogenerated charge transfer and eliminating interface recombination. The resulting JLMT PSCs exhibited significantly improved photovoltaic performance and reduced hysteresis behavior, achieving a champion PCE of 21.76% accompanied by a $V_{oc}$ of 1.20 V. Meanwhile, the PCE retained 93% of its value under room temperature conditions with a relative humidity of 30% compared with the control devices after 30 days. Compared with the current mainstream interface passivation approaches, this study highlights the potential of the interface templating approach for enhancing the efficiency and stability of perovskite solar cells.

## Conflicts of interest

There are no conflicts of interest to declare.

## Acknowledgements

The authors gratefully acknowledge the support from the National Natural Science Foundation of China (Grant No. 62275101, 22075101 and 11904127), Program for the development of Science and Technology of Jilin province (Item No. YDZJ202201ZYTS300 and 20210509050RQ), Program for the Science and Technology of Education Department of Jilin Province (Item No. JJKH20220440KJ).

## References

1 M. Kim, J. Jeong, H. Lu, T. K. Lee, F. T. Eickemeyer, Y. Liu, I. W. Choi, S. J. Choi, Y. Jo, H.-B. Kim, S.-I. Mo, Y.-K. Kim,

H. Lee, N. G. An, S. Cho, W. R. Tress, S. M. Zakeeruddin, A. Hagfeldt, J. Y. Kim, M. Grätzel and D. S. Kim, Conformal quantum dot-$SnO_2$ layers as electron transporters for efficient perovskite solar cells, *Science*, 2022, **375**, 302–306.

2 Best Research-Cell Efficiency Chart, Photovolataic Research NREL, **https://ww.nrel.gov/pv/cell-efficency.html**.

3 D. Zheng, R. Peng, G. Wang, J. L. Logsdon, B. Wang, X. Hu, Y. Chen, V. P. Dravid, M. R. Wasielewski, J. Yu, W. Huang, Z. Ge, T. J. Marks and A. Facchetti, Simultaneous bottomup interfacial and bulk defect passivation in highly efficient planar perovskite solar cells using nonconjugated small-molecule electrolytes, *Adv. Mater.*, 2019, **31**, 1903239.

4 Z. Cao, X. Deng, S. Wang, Y. Yuan, Y. Chen, Z. Wang, Y. Liu, L. Ding and F. Hao, Metal oxides alternatives for efficient electron transport in perovskite solar cells: beyond $TiO_2$ and $SnO_2$, *J. Mater. Chem. A*, 2020, **8**, 19768–19787.

5 Z. Wang, Y. Huo, H. Li and L. Wang, Formation, detection, and function of oxygen vacancy in metal oxides for solar energy conversion, *Adv. Funct. Mater.*, 2022, **32**, 2109503.

6 L. Yang, Z. Liu, Y. Duan, S. Zhan, S. Yang, K. He, Y. Li, Y. Zhou, N. Yuan, J. Ding and S. (Frank) Liu, Record-efficiency flexible perovskite solar cells enabled by multi-functional organic ions interface passivation, *Adv. Mater.*, 2022, **34**, 2201681.

7 T. Li, X. Wang, J. Shi, Y. Wang, J. Yang and Q. Zhang, Grain size and interface modification via cesium carbonate post treatment for efficient $SnO_2$-based planar perovskite solar cells, *ACS Appl. Energy Mater.*, 2021, **4**, 7002–7011.

8 F. Tan, H. Tan, J. Z. Fan, Y. Wang, S. Yue, X. Wang, Z. Shen, S. Li, J. Kim, Y. Gao, G. Yue, R. Liu, Z. Huang, C. Dong, X. Hu, W. Zhang, Z. Wang, S. Qu, Z. Wang and E. H. Sargent, Dual coordination of Ti and Pb using bilinkable ligands improves perovskite solar cell performance and stability, *Adv. Funct. Mater.*, 2020, **30**, 2005155.

9 L. Zuo, N. D. Marco, Y.-T. Hsieh, H. ChenOrcid, P. Sun, S.-Y. Chang, H. Zhao, S. Dong and Y. Yang, Tailoring the interfacial chemical interaction for high efficiency perovskite solar cells, *Nano Lett.*, 2017, **17**, 269–275.

10 J. Du, L. Feng, X. Guo, X. Huang, Z. Lin, J. Su, Z. Hu, J. Zhang, J. Chang and Y. Hao, Enhanced efficiency and stability of planar perovskite solar cells by introducing amino acid to $SnO_2$/perovskite interface, *J. Power Sources*, 2020, **455**, 227974.

11 H. Zou, X. Meng and X. Zhao, Hofmeister Effect-Enhanced Hydration Chemistry of Hydrogel for High-Efficiency Solar-Driven Interfacial Desalination, *Adv. Mater.*, 2023, **35**, 202207262.

12 X. Zhao, X. Meng, H. Zou, Z. Wang, Y. Du, Y. Shao, J. Qin and J. Qiu, Topographic Manipulation of Graphene Oxide by Polyaniline Nanocone Arrays Enables High-Performance Solar-Driven Water Evaporation, *Adv. Funct. Mater.*, 2023, **33**, 2209207.

13 X. Zhao, X. Meng, H. Zou, Y. Zhang, Y. Ma, Y. Du, Y. Shao, J. Qi and J. Qiu, Nano-enabled solar driven-interfacial evaporation: Advanced design and opportunities, *Nano Res.*, 2023, **16**, 6015–6038.

14 X. Meng, C. Yu, X. Song, J. Iocozzia, J. Hong, M. Rager, H. Jin, S. Wang, L. Huang, J. Qiu and Z. Lin, Scrutinizing Defects and Defect Density of Selenium-Doped Graphene for High-Efficiency Triiodide Reduction in Dye-Sensitized Solar Cells, *Angew. Chem., Int. Ed.*, 2018, **57**, 4682–4686.

15 Y. Ma, X. Meng, K. Li, L. Zhang, Y. Du, X. Cai and J. Qiu, Scrutinizing Synergy and Active Site of Nitrogen and Selenium Dual-Doped Porous Carbon for Efficient Triiodide Reduction, *ACS Catal.*, 2023, **13**, 1290–1298.

16 F. Wang, Y. Zhang, M. Yang, J. Du, L. Xue, L. Yang, L. Fan, Y. Sui, J. Yang and X. Zhang, Exploring low-temperature processed a-$WO_x$/$SnO_2$ hybrid electron transporting layer for perovskite solar cells with efficiency >20.5%, *Nano Energy*, 2019, **63**, 103825.

17 C. H. Lee, T. Schiros, E. J. Santos, B. Kim, K. G. Yager, S. J. Kang, S. Lee, J. Yu, K. Watanabe, T. Taniguchi, J. Hone, E. Kaxiras, C. Nuckolls and P. Kim, Epitaxial growth of molecular crystals on van der Waals substrates for high-performance organic electronics, *Adv. Mater.*, 2014, **26**, 2812–2817.

18 X. Li, L. Basile, B. Huang, C. Ma, J. Lee, I. V. Vlassiouk, A. A. Puretzky, M.-W. Lin, M. Yoon, M. Chi, J. C. Idrobo, C. M. Rouleau, B. G. Sumpter, D. B. Geohegan and K. Xiao, van der Waals epitaxial growth of two-dimensional single-crystalline GaSe domains on graphene, *ACS Nano*, 2015, **9**, 8078–8088.

19 R. Wu, Q. Tao, W. Dang, Y. Liu, B. Li, J. Li, B. Zhao, Z. Zhang, H. Ma, G. Sun, X. Duan and X. Duan, van der Waals epitaxial growth of atomically thin 2D metals on dangling–bond–free $WSe_2$ and $WS_2$, *Adv. Funct. Mater.*, 2019, **29**, 1806611.

20 T. Wang, F. Zheng, G. Tang, J. Cao, P. You, J. Zhao and F. Yan, 2D $WSe_2$ flakes for synergistic modulation of grain growth and charge transfer in tin-based perovskite solar cells, *Adv. Sci.*, 2021, **8**, 2004315.

21 G. Tang, P. You, Q. Tai, A. Yang, J. Cao, F. Zheng, Z. Zhou, J. Zhao, P. K. L. Chan and F. Yan, Solution-phase epitaxial growth of perovskite films on 2D material flakes for high-performance solar cells, *Adv. Mater.*, 2019, **31**, 1807689.

22 N. A. Abd Malek, N. Alias, S. K. Md Saad, N. A. Abdullah, X. Zhang, X. Li, Z. Shi, M. M. Rosli, T. H. Tengku Abd Aziz, A. A. Umar and Y. Zhan, Ultra-thin $MoS_2$ nanosheet for electron transport layer of perovskite solar cells, *Opt. Mater.*, 2020, **104**, 109933.

23 L. C. Palilis, M. Vasilopoulou, A. Verykios, A. Soultati, E. Polydorou, P. Argitis, D. Davazoglou, A. R. B. Mohd Yusoff and M. K. Nazeeruddin, Inorganic and hybrid interfacial materials for organic and perovskite solar cells, *Adv. Energy Mater.*, 2020, **10**, 2000910.

24 P. Zhang, Z. Wang, L. Liu, L. H. Klausen, Y. Wang, J. Mi and M. Dong, Modulation the electronic property of 2D monolayer $MoS_2$ by amino acid, *Appl. Mater. Today*, 2019, **14**, 151–158.

25 D. Kiriya, M. Tosun, P. Zhao, J. S. Kang and A. Javey, Air-stable surface charge transfer doping of $MoS_2$ by benzyl viologen, *J. Am. Chem. Soc.*, 2014, **136**, 7853–7856.

 

26 J. Li, T. He, Y. Zhao, X. Zhang, W. Zhong, X. Zhang, J. Ren and Y. Chen, *In situ* N-doped ultrathin $MoS_2$ anchored on N-doped carbon nanotubes skeleton by Mo-N bonds for fast pseudocapacitive sodium storage, *J. Alloys Compd.*, 2022, **897**, 163170.
27 Y. Pang, S. Zhang, L. Liu, J. Liang, Z. Sun, Y. Wang, C. Xiao, D. Ding and S. Ding, Few-layer $MoS_2$ anchored at nitrogen-doped carbon ribbons for sodium-ion battery anodes with high rate performance, *J. Mater. Chem. A*, 2017, **5**, 17963–17972.
28 K. Mahmood, A. Khalid, S. W. Ahmad, H. G. Qutab, M. Hameed and R. Sharif, Electrospray deposited $MoS_2$ nanosheets as an electron transporting material for high efficiency and stable perovskite solar cells, *Sol. Energy*, 2020, **203**, 32–36.
29 P. Huang, Z. Wang, Y. Liu, K. Zhang, L. Yuan, Y. Zhou, B. Song and Y. Li, Water-soluble 2D transition metal dichalcogenides as the hole-transport layer for highly efficient and stable p-i-n perovskite solar cells, *ACS Appl. Mater. Interfaces*, 2017, **9**, 25323–25331.
30 J. Cao, G. Tang, P. You, T. Wang, F. Zheng, J. Zhao and F. Yan, Enhanced performance of planar perovskite solar cells induced by van der Waals epitaxial growth of mixed perovskite films on $WS_2$ flakes, *Adv. Funct. Mater.*, 2020, **30**, 2002358.
31 B.-B. Cui, N. Yang, C. Shi, S. Yang, J.-Y. Shao, Y. Han, L. Zhang, Q. Zhang, Y.-W. Zhong and Q. Chen, Naphtho [1,2-b:4,3-b']dithiophene-based hole transporting materials for high-performance perovskite solar cells: molecular engineering and opto-electronicproperties, *J. Mater. Chem. A*, 2018, **6**, 10057–10063.
32 W. Xing, Y. Chen, X. Wang, L. Lv, X. Ouyang, Z. Ge and H. Huang, $MoS_2$ quantum dots with a tunable work function for high-performance organic solar cells, *ACS Appl. Mater. Interfaces*, 2016, **8**, 26916–26923.
33 Y. Du, H. Liu, A. T. Neal, M. Si and P. D. Ye, Molecular doping of multilayer $MoS_2$ field-effect transistors: reduction in sheet and contact resistances, *IEEE Electron Device Lett*, 2013, **34**, 1328–1330.
34 P. Rastogi, S. Kumar, S. Bhowmick, A. Agarwal and Y. S. Chauhan, Doping strategies for monolayer $MoS_2$ via surface sdsorption: A systematic study, *J. Phys. Chem. C*, 2014, **118**, 30309–30314.
35 S. McDonnell, R. Addou, C. Buie, R. M. Wallace and C. L. Hinkle, Defect-dominated doping and contact resistance in $MoS_2$, *ACS Nano*, 2014, **8**, 2880–2888.
36 L. Zhu, X. Zhang, M. Li, X. Shang, K. Lei, B. Zhang, C. Chen, S. Zheng, H. Song and J. Chen, Trap state passivation by rational ligand molecule engineering toward efficient and stable perovskite solar cells exceeding 23% Efficiency, *Adv. Energy Mater.*, 2021, **11**, 2100529.
37 Y. Liu, J. Yin, Y. Zhou, L. Sun, W. Yue, Y. Sun and Y. Wang, Tuning electron transport direction through the deposition sequence of $MoS_2$ and $WS_2$ on fluorine–doped tin oxide for improved electrocatalytic reduction efficiency, *ChemElectroChem*, 2019, **6**, 2737–2740.
38 T.-H. Su and Y.-J. Lin, Effects of nitrogen plasma treatment on the electrical property and band structure of few-layer $MoS_2$, *Appl. Phys. Lett.*, 2016, **108**, 033103.
39 X. Ding, X. Cui, A. Sohail, P. P. Murmu, J. Kennedy, N. Bao, J. Ding, R. Liu, M. Peng, L. Wang, X. Chu, A. Vinu, S. P. Ringer and J. Yi, Defects engineering induced ultrahigh magnetization in rare earth element Nd–doped $MoS_2$, *Adv. Quantum Technol.*, 2020, **4**, 2000093.
40 H. Ying, X. Li, H. Wang, Y. Wang, X. Hu, J. Zhang, X. Zhang, Y. Shi, M. Xu and Q. Zhang, Band structure engineering in $MoS_2$ based heterostructures toward high–performance phototransistors, *Adv. Opt. Mater.*, 2020, **8**, 2000430.
41 F. Wang, X. Li, J. Du, H. Duan, H. Wang, Y. Gou, L. Yang, L. Fan, J. Yang and F. Rosei, Coordinating light management and advance metal nitride interlayer enables $MAPbI_3$ solar cells with >21.8% efficiency, *Nano Energy*, 2022, **92**, 106765.
42 F. Wang, Y. Zhang, M. Yang, D. Han, L. Yang, L. Fan, Y. Sui, Y. Sun, X. Liu, X. Meng and J. Yang, Interface dipole induced field–effect passivation for achieving 21.7% efficiency and stable perovskite solar cells, *Adv. Funct. Mater.*, 2020, **31**, 2008052.